



Quantum dot-based broadband optical antenna for efficient extraction of single photons in the telecom O-band

JINGZHONG YANG,^{1,5}  CORNELIUS NAWRATH,^{2,5} ROBERT KEIL,³ RAPHAEL JOOS,² XI ZHANG,³ BIANCA HÖFER,³ YAN CHEN,³ MICHAEL ZOPF,¹ MICHAEL JETTER,² SIMONE LUCA PORTALUPI,² FEI DING,^{1,3,6} PETER MICHLER,^{2,7} AND OLIVER G. SCHMIDT^{3,4}

¹Institut für Festkörperphysik, Leibniz Universität Hannover, Appelstraße 2, 30167 Hannover, Germany

²Institut für Halbleiteroptik und Funktionelle Grenzflächen, Center for Integrated Quantum Science and Technology (IQST) and SCoPE, University of Stuttgart, Allmandring 3, 70569 Stuttgart, Germany

³Institute for Integrative Nanosciences, Leibniz IFW Dresden, Helmholtzstraße 20, 01069 Dresden, Germany

⁴Material Systems for Nanoelectronics, Technische Universität Chemnitz, 09107 Chemnitz, Germany

⁵Equally contributed

⁶f.ding@fkp.uni-hannover.de

⁷p.michler@ihfg.uni-stuttgart.de

Abstract: Long-distance fiber-based quantum communication relies on efficient non-classical light sources operating at telecommunication wavelengths. Semiconductor quantum dots are promising candidates for on-demand generation of single photons and entangled photon pairs for such applications. However, their brightness is strongly limited due to total internal reflection at the semiconductor/vacuum interface. Here we overcome this limitation using a dielectric antenna structure. The non-classical light source consists of a gallium phosphide solid immersion lens in combination with a quantum dot nanomembrane emitting single photons in the telecom O-band. With this device, the photon extraction is strongly increased in a broad spectral range. A brightness of 17 % (numerical aperture of 0.6) is obtained experimentally, with a single photon purity of $g^{(2)}(0) = 0.049 \pm 0.02$ at saturation power. This brings the practical implementation of quantum communication networks one step closer.

© 2020 Optical Society of America under the terms of the [OSA Open Access Publishing Agreement](#)

1. Introduction

Non-classical light sources are an essential element for secure photonic quantum information processing [1], quantum cryptography [2] or distributed quantum networks [3,4]. Photons exhibit high stability against dephasing caused by the environment and can be transmitted over long distances with standard optical fibers. Semiconductor quantum dots (QDs) can deterministically emit photons in the telecom wavelength bands around 1.31 μm [5–10] and 1.55 μm [11–17], at which chromatic dispersion and transmission losses in optical fibers are at a respective minimum [18]. However, the high refractive index of the surrounding semiconductor results in total internal reflection (TIR) at the semiconductor/vacuum interface, thereby confining most of the photons in the host material [19,20].

Various approaches have been investigated in the last few years to enhance the extraction efficiency of QD emission in the wavelength range from 700 nm to 900 nm [21]. Making use of cavity quantum electrodynamics (cQED), the photons are efficiently emitted in the limited spectral width of the cavity mode. Multifarious nanoscale structures are developed in that regard, such as micropillars [22–25] or circular Bragg gratings [26,27]. Brightness values of up to 85 % have been observed in combination with high single-photon purity [28]. Moreover, the

cavity-induced Purcell effect shortens the radiative lifetimes of the emitters, resulting in improved photon indistinguishabilities on short time scales [28,29].

Another approach is to modify the photonic environment of the QDs, e.g. by embedding them in nanowires [30,31] or making use of microlenses [7,32–35]. This allows for a broadband and efficient extraction of photons from the semiconductor material. Alternatively, metal nanostructures can be placed close to the emitter [36,37] which results in photoluminescence enhancement and directional emission by utilizing the localized surface plasmon resonance.

These approaches generally require deterministic fabrication methods to ensure high yield and ideal performances, thereby increasing the overall fabrication complexity [34,38,39]. Recently, a new approach called dielectric antenna has been realized with GaAs/AlGaAs QDs grown by molecular beam epitaxy [40]. Based on a solid immersion lens (SIL) and the well-established fabrication of QD-containing nanomembranes, an emission brightness of up to 65 % was obtained for single photons emitted around 780 nm.

Increasing the photon extraction for QDs emitting in the telecom O-band has been investigated using nanowires and micropillars, with a brightness of up to 3.3 % [9,41]. Using nanophotonic cavities, 36 % brightness in a narrow-band wavelength range was reported [5]. While this approach is also expected to be beneficial for the indistinguishability on short time scales, the resulting linewidth broadening could cause photon wave-packet dispersion during long-haul propagation, in particular in the near-infrared and also in the telecom C-band [42,43]. With a mesa structure on top of the emitter, a brightness of 10 % has been experimentally realized in a broad wavelength range, but the position misalignment between the structure and the emitter significantly reduces the extraction efficiency [44]. Besides, deterministic Gaussian-shaped microlenses fabricated via chemical etching were estimated to reach up to 17 % brightness. This method requires the use of sophisticated techniques with high accuracy and fabrication quality [7]. In this letter, we present a dielectric antenna structure extracting single photons in the telecom O-band from InGaAs/GaAs QDs grown via metal-organic vapor-phase epitaxy (MOVPE). Based on simulations to optimize the antenna structure design, we experimentally fabricate and characterize this device. Compared to the as-grown sample, a 40 times brighter single-photon source is realized over a broadband spectral range, while maintaining a high single-photon purity.

2. Device fabrication

The InGaAs/GaAs QDs are grown by MOVPE, which is commonly employed for commercial semiconductor fabrication purposes. With careful optimization of the strain in the low-density QDs, photon emission in the telecom O-band has been realized [45]. The initial GaAs (001) substrate is overgrown with a 50 nm buffer layer, followed by 100 nm AlGaAs, acting as a sacrificial layer for the intended membrane processing. The subsequent membrane structure consists of 190 nm GaAs, followed by InGaAs QDs which are embedded in a strain-reducing layer. The QDs are then capped with a 266 nm GaAs layer [46].

Figure 1 shows the fabrication procedure of the dielectric antenna device consisting of a commercial gallium phosphide (GaP) semi-spherical solid immersion lens, a nanomembrane containing InGaAs/GaAs QDs and a silicon carrier substrate. As shown in Fig. 1(a), a droplet of polymethyl methacrylate (PMMA) is deposited on the flat surface of a SIL with a diameter of 2 mm. Spin coating is then performed with a rotation speed of 7000 rpm, yielding a PMMA layer thickness of ~ 100 nm. To obtain a single nanomembrane containing QDs, a sequence of well-established fabrication methods is employed to the as-grown sample [40]. A square array of $160\ \mu\text{m} \times 120\ \mu\text{m}$ -sized rectangular metal pads is defined, by means of photolithography, followed by the deposition of 4 nm chromium and 100 nm gold and a subsequent lift-off process. Next, a solution of sulfuric acid, hydrogen peroxide and deionized water (ratio 1:8:200) is applied to vertically etch the substrate in order to expose the AlGaAs sacrificial layer. The latter is

then removed using 25 % hydrofluoric acid solution to create free-standing membranes [40,47]. One single nanomembrane is transferred onto the bottom center of the SIL, with the PMMA layer acting as glue. Placing the whole structure on a silicon substrate (Fig. 1(c)) for convenient handling completes the device fabrication. The TIR at the semiconductor nano-membrane surface is greatly alleviated in this dielectric antenna structure due to the close contact of the nano-membrane ($n_{\text{GaAs}} \approx 3.40$) and the high refractive index GaP SIL ($n_{\text{GaP}} \approx 3.14$).

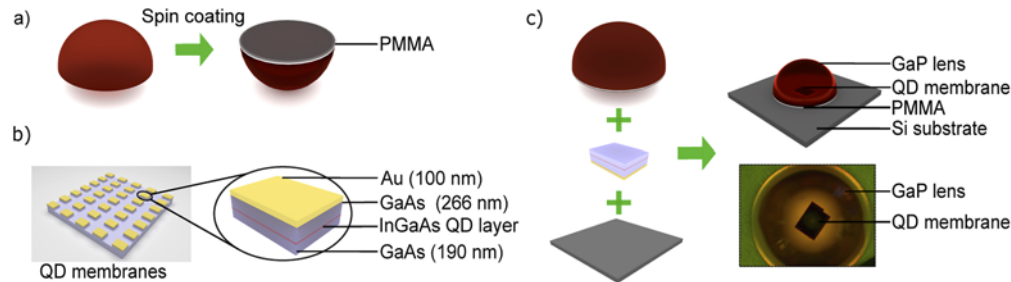


Fig. 1. Fabrication steps of the telecom O-band dielectric antenna. (a) PMMA deposited on the flat surface of the GaP SIL. (b) Free-standing nanomembranes remain on the substrate after photolithography and wet chemical etching. The structure of a single nanomembrane is shown (right) (c) Combining the SIL, QD-nanomembrane and the silicon substrate (left), a dielectric antenna device is constructed (top right). The image taken by optical microscopy displayed in the bottom right corner shows the single nanomembrane glued centrally to the bottom of the SIL.

3. Results and discussion

3.1. Evaluation of the brightness

To demonstrate the effectiveness of the device, we characterized the spectra and wavelength statistics of the as-grown sample and dielectric antenna, respectively. In Fig. 2(a), the spectra of two typical QDs are shown. A remarkable brightness enhancement is observed for the dielectric antenna. To demonstrate that the device fabrication only has a small effect on the emission wavelength, the QD emission in the dielectric antenna and as-grown sample is characterized. According to the wavelength statistics of the samples shown in the panel (b) of Fig. 2, the histograms show a similar central wavelength. Apart from possible fabrication-related effects like a difference in the strain situation in the surrounding of the QDs due to the change from a bulk sample to a nano-membrane, the 10 nm red-shift is ascribed to an inhomogeneity of QD sizes over the sample and the different subsets of randomly chosen QDs for the characterization.

Furthermore, we study the power-dependent photoluminescence under above-band excitation, using a pulsed laser at 633 nm with a repetition rate of 80 MHz (Fig. 2(c)). The recorded photon counts are obtained by integrating the brightest transition peak shown on the CCD of the spectrometer. Considering the system loss, we can calculate the number of photons arriving at the objective in the photoluminescence measurement setup. Now we determine the brightness enhancement caused by the dielectric antenna: The photon count rate from 10 QDs in the as-grown sample, excited under saturation power P_0 , is averaged. Then the enhancement factor is given by the ratio between the photon counts of each characterized QD (in total 57) in the device and the value from the as-grown sample. The rate of collected photons is increased by up to two orders of magnitude compared to the as-grown sample. On average, the brightness is enhanced by more than a factor of 40 as displayed in the panel (d) of Fig. 2.

So far, we considered only the dominant peak of the photoluminescence spectrum. In order to determine the brightness, i.e. the average number of photons emitted from the sample per

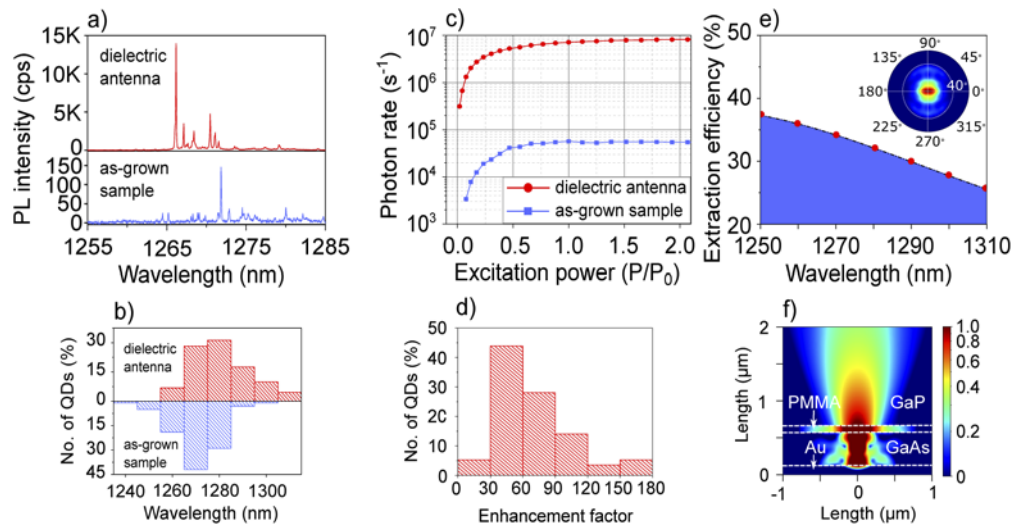


Fig. 2. Characterization of the dielectric antenna sample. (a) Exemplary QD emission spectra from the dielectric antenna and the as-grown sample. (b) The wavelength distribution before and after the processing, for which 131 and 100 QDs are characterized, respectively. (Red: dielectric antenna; Blue: as-grown sample). (c) Number of photons arriving at the objective as a function of excitation power for two exemplary QDs. The photon rate is determined by integrating the counts of the brightest transition peak shown on the CCD and correcting for the system losses. (d) The statistics of the brightness enhancement factor comparing the dielectric antenna (57 QDs) and the as-grown sample. (e) Simulated extraction efficiency as a function of the emission wavelength. The inset shows the polar view of the device radiation in the far-field. (f) The side view of the electric field intensity distribution in the dielectric antenna.

excitation cycle, the emission from other excitonic states has to be taken into account. In the experiment, all the dominant transition lines of the brightest QD emission (labeled QD2 in Fig. 3(b)) are identified. Under pulsed above-band excitation, all photons emitted from independent excitonic decay channels are included. A brightness of 17% is obtained in a conservative estimate for an objective numerical aperture (NA) of 0.6, considering corrections for background emission and multiphoton contributions (see Appendix A.3).

To verify further that the device operates in a broad wavelength range, we perform finite-difference time-domain (FDTD) simulations of the device. First, we study the extraction efficiency as a function of the PMMA layer thickness under the assumption of a 1.31 μm emission from a horizontally oscillating dipole source (see Appendix A.1). This is done because the low refractive index PMMA spacer does not only serve as a glue, but it also changes the emission pattern of the dielectric antenna in the far-field, influencing the extraction efficiency for a limited objective NA [40]. The following simulations are performed with a PMMA layer thickness of 100 nm and do not include an anti-reflection coating on the GaP lens, which is in accordance with the fabricated device. This thickness was found to be more controllable and reproducible than larger thicknesses in the fabrication procedure. The polar view of the device radiation in the far-field (inset in Fig. 2(e)) manifests that the majority of photons can be collected within a polar angle of 40 degrees. Finally, the extraction efficiency of photons as a function of the emission wavelength is determined in the far-field, considering a NA of 0.6. In a wavelength range of 60 nm in which the QD ensemble is emitting, the dielectric antenna increases the photon extraction performance. This is much broader than cQED approaches, which usually enhance the emission in a spectral window of a few nm [5,22,24]. The far-field emission profile of the electric field is calculated.

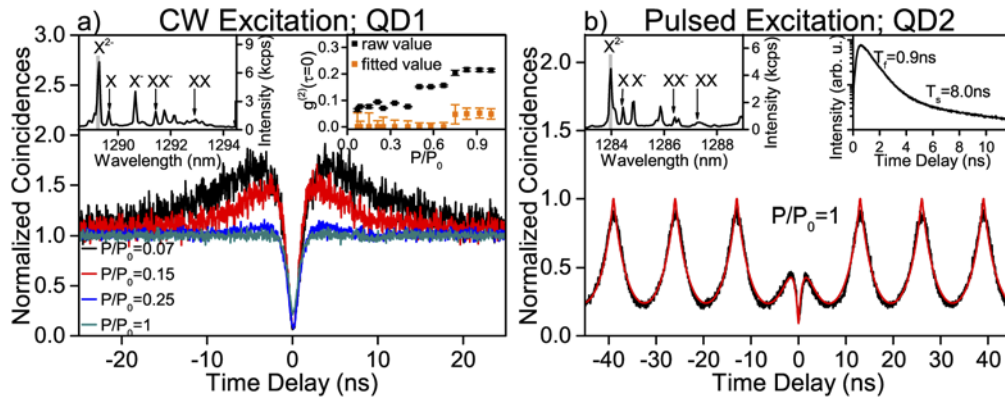


Fig. 3. Measurements on the X^{2-} transition of QD1 and QD2 (spectra shown in the insets with the grey rectangle indicating the width of the spectral transmission window used for selecting individual transitions): (a) Second-order correlation measurements under continuous wave excitation for different pump powers. Inset: Single-photon purity as a raw value and after fitting (including the deconvolution with the system response function). (b) Pulsed second-order correlation measurement at saturation power with a fit function. The inset shows the time-resolved fluorescence measurement on a semi-logarithmic scale.

Panel (f) of Fig. 2 shows the electric field intensity distribution of the dielectric antenna in a side view. A strong and directional emission pattern is observed in the GaP, indicating an increased photon extraction from the substrate. Nevertheless, there is a difference between the extraction efficiency obtained from theoretical calculations and the experimentally determined brightness. Note that these values can only be compared assuming a unity state preparation fidelity and negligible non-radiative decay channels [21]. Further possible reasons for the discrepancy include the roughness of the lens surface and the uncertainty of the PMMA layer thickness. Moreover, due to the overall low density of quantum emitters in the sample, only a few QDs are located in the very center of the GaP SIL in which the device is expected to perform optimally. Therefore, the observed dots provide a lower bound of the determined brightness.

3.2. Evaluation of the single-photon purity

On the processed dielectric antenna sample, two bright QDs, labeled QD1 and QD2, are characterized in-depth regarding their single-photon purity under different pumping conditions to assess their suitability as single-photon sources. All measurements are performed under above-band excitation, creating free charge carriers in the barrier material. First, the most prominent spectral lines are assigned to the respective excitonic states, as shown in the insets of Figs. 3(a) and (b). This allocation is based on power- and polarization-dependent micro-photoluminescence series, time-resolved fluorescence and second-order cross-correlation measurements together with previous experimental and theoretical investigations on corresponding planar samples [45,48,49]. The most prominent spectral features result from charged excitonic states suggesting a background doping of the sample.

Next, the single-photon purity of the QDs is evaluated using a Hanbury-Brown and Twiss setup. The second-order correlation function $g^{(2)}(\tau)$ is measured under continuous-wave (cw) and pulsed excitation for different pump powers. The brightest transition at medium excitation powers, namely the double negatively charged exciton (X^{2-}), is investigated. As shown in Fig. 3(a), the expected antibunching dip at zero time delay for cw auto-correlation measurements is well preserved up to saturation. For 7% of the saturation power P_0 , the raw value excluding a correction for residual background emission yields $g_{\text{raw}}^{(2)}(0) = 0.063 \pm 0.005$, while for $P/P_0 = 1$

a value of $g_{\text{raw}}^{(2)}(0) = 0.214 \pm 0.006$ is obtained as displayed in the inset of Fig. 3(a). The uncertainty is obtained from the normalized standard deviation of the Poissonian level. This increase is attributed to the larger spectral background contribution at higher excitation powers. A bunching effect at small, non-zero time delays, observed for low excitation powers, becomes more pronounced for decreasing pump powers while exhibiting an increase of the corresponding time constant. This is attributed to the background doping and charge carrier trap states from which the QD can be refilled [50–53] after an initial excitation and emission event. This assumption is corroborated by a time-resolved fluorescence measurement of this transition (see Appendix A.2) yielding two decay constants $T_f = 1.1$ ns and $T_s = 15.8$ ns. The same qualitative behaviour can be seen for QD2, as displayed in the inset of Fig. 3(b). While the fast decay constant is connected to the radiative lifetime of the transition, the secondary decay yields information on the time scale of the refilling process. Possible spin flips are excluded for the X^{2-} transition since it does not have a dark state. At low excitation powers, the possibility of refilling a QD on short time scales after an initial emission increases the probability of detecting two photons on these time scales i.e. yields values larger than the Poissonian level for small-time delays. At higher pump powers, this effect is no longer observed because a charge carrier reservoir created by the strong above-band excitation is large enough to provide carriers on all time scales.

To precisely estimate the single-photon purity, the data are fitted including a deconvolution with the system response function that is obtained from the auto-correlation of a 3 ps laser pulse. For the measurements with apparent bunching, this effect is included in the fit function [54,55]. The values for $g^{(2)}(0)$ are displayed in the inset of Fig. 3(a), where the uncertainties are calculated via error propagation from the 1σ confidence bounds of the fit parameters determined by the non-linear fit algorithm. Even at saturation power, a value of $g^{(2)}(0) = 0.049 \pm 0.020$ is determined. For values below $P/P_0 = 0.75$ any residual two-photon contribution falls below the accuracy of the measurement and fit procedure, i.e. the excellent single-photon properties of the QDs [48] are not affected by the fabrication of the dielectric antenna.

While the single-photon purity is characterized by the evaluation of the $g^{(2)}(\tau)$ function under cw pumping, the suitability of the QDs for applications based on triggered single photons is evaluated by second-order correlation measurements under pulsed excitation. This is obtained by exciting the QD with a pulsed laser centered at 670 nm with a repetition rate of 76.9 MHz. The result of this measurement for the X^{2-} transition of QD2 in saturation is displayed in Fig. 3(b) alongside a fit function. Due to the overlap of neighboring peaks separated by the repetition period of $\tau_{\text{rep}} = 13$ ns the signal does not decay to zero. Additionally, the above-mentioned refilling effect leads to a secondary radiative decay with a decay constant of 8.0 ns as observed in the time-resolved fluorescence measurement displayed in the inset of Fig. 3(b). This effect also explains the residual peak around zero time delay of the pulsed intensity auto-correlation measurement [56]. An antibunching dip owing to the single-photon nature of the emitted light is superimposed on this residual peak [50–53,55]. Hence, multi-photon emission events at vanishing time delays are strongly suppressed. A secondary emission event within a time period smaller than the repetition time τ_{rep} due to refilling, is found with a probability between 50 % and 70 % depending on the pump powers. Note that, for low excitation power a bunching of the first peaks at multiples of τ_{rep} is found and included in the respective fit functions. In other words, the QDs exhibit excellent single-photon emission properties but their suitability as a single-photon turnstile device [57] is limited by charge carriers refilling the QD [56]. This effect is accounted for when determining the extraction efficiency [58].

Individual QDs [51] in spatial proximity to a charge carrier trap state have been found to be prone to refilling [45,50–53,55,56]. Considering the overall low spatial density of QDs [45] and the size of the area in which the SIL enhances the extraction efficiency optimally, the study at hand is limited to the investigation of these QDs. Hence, the refilling effect is assumed to be a property of the individual QDs under investigation rather than related to the transfer of the

dielectric antenna approach to InGaAs QDs emitting in the telecom O-band. As an improvement for the next sample generation, we propose to adapt the growth parameters to increase QD density and counteract the doping to reduce the refilling effect. With this, the number of available QDs as prospective bright sources of triggered, single photons in the telecom O-band will be enhanced.

4. Conclusion

We fabricated a dielectric antenna structure based on a GaP SIL, enhancing the extraction efficiency of InGaAs/GaAs QDs emitting in the technologically important telecom O-band. The brightness is experimentally determined to 17 % for an objective NA of 0.6. FDTD simulations suggest a maximum extraction efficiency of up to 38 % for the same NA and a structure with optimal PMMA layer thickness and low surface roughness of the SIL and QD membrane. Depositing an appropriately designed anti-reflection coating layer on the curved SIL surface can further enhance the brightness. The fabrication process of the dielectric antenna structure does not significantly alter the emission wavelength of the QDs. In-depth investigations of the transition lines of the two brightest QDs consistently point to a background doping and related charge carrier refilling effects. In order to exploit the demonstrated excellent single-photon purity values under cw excitation for single-photon turnstile operation, quasi-resonant or resonant excitation schemes should be employed.

Appendices

A.1. FDTD simulation method for the dielectric antenna

The simulation of the dielectric antenna is performed by the commercial finite difference time domain (FDTD) software offered by Lumerical Solutions Inc. In the simulation, a three-dimensional simulation structure of the dielectric antenna is constructed according the sketch depicted in Fig. 4(a). The wavelength-dependent refractive indices of Au, Cr, GaAs are provided by the software. The refractive index of PMMA is taken from the manufacturer's specification. The refractive index of GaP around 1.31 μm is taken from [59]. To ensure the accurate simulation result, a mesh accuracy of 6 with an auto non-uniform mesh type is used in the simulation settings, corresponding to mesh grid size of a 26th of the minimal wavelength [60]. The perfectly matched layer boundary condition for the x/y/z axes for the simulation area under consideration is applied. A mesh grid of $5 \times 5 \times 5 \text{ nm}^3$ is used to ensure sufficient precision at the interfaces between the multi-layers. An in-plane polarized dipole source is embedded in the GaAs layer with the wavelength range from 1.25 to 1.31 μm .

Figure 4(b) shows the far-field extraction efficiency for different objective NAs as a function of PMMA layer thickness for the dielectric antenna operating at 1.31 μm used in this work. The efficiency is calculated using a monitor embedded in the GaP, considering only the radiation angle range determined by the NA. The reflection at the GaP/vacuum interface is taken into account by applying Fresnel equations. When the PMMA layer thickness is 0 nm, there is no antenna effect but only the lensing, which means the photons will spread over the full solid angle in the far-field. Therefore, the extraction efficiency is only determined by the NA of the objective. As shown in the figure, the device performs best with the extraction efficiency enhancement for a PMMA layer thickness of ~ 290 nm but lower than the case of 0 nm due to the antenna effect. This is ascribed by the partial total internal reflection at the GaAs-PMMA interface. The antenna effect starts to vanish for a PMMA layer thickness larger than 290 nm. The PMMA layer thickness for the simulations described in the main text is 100 nm in accordance with the fabricated device. We tried to reduce the PMMA layer thickness to the minimum since obtaining a precise thickness by spin-coating on a small GaP SIL (2 mm diameter) is easier for lower thicknesses.

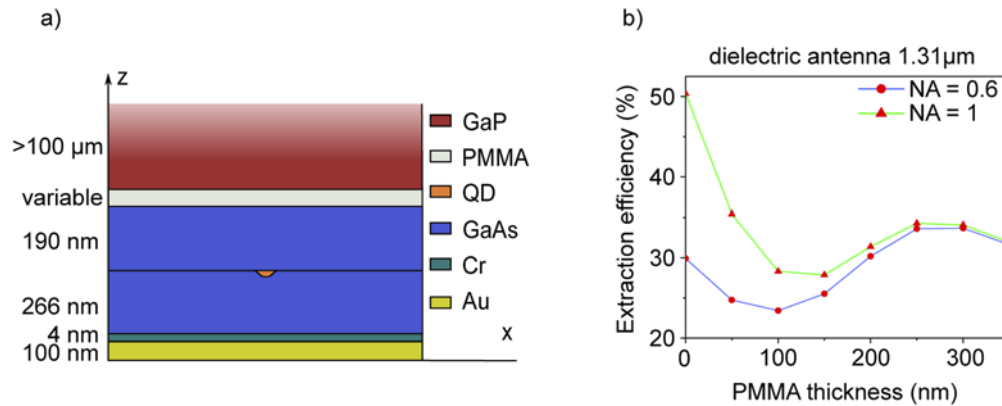


Fig. 4. Simulation of the dielectric antenna. (a) Schematic of the simulation structure. (b) Simulation results for the device operating at 1.31 μm used in this work. The far-field extraction efficiency is shown over the PMMA layer thickness for different NAs of the collection optics.

A.2. Complementary correlation measurements of QD1 and QD2

To complement the measurement data shown in the main text, the second-order correlation measurement under continuous-wave excitation is shown in Fig. 5 for the quantum dot labeled QD2 in the manuscript. The measurements were conducted for excitation powers P between 60% and 100% of the saturation power P_0 , of which these two extreme cases are depicted.

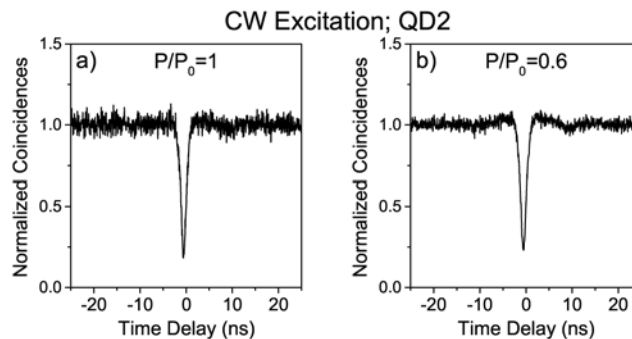


Fig. 5. Second-order correlation functions under continuous-wave excitation for the quantum dot labeled QD2 in the main text at (a) $P/P_0 = 1$ and (b) $P/P_0 = 0.6$ of the saturation power P_0 .

Furthermore, correlation measurements under pulsed excitation of QD1 are shown in Fig. 6. Panel (a) depicts the time-resolved photoluminescence measurement in a semi-logarithmic plot with the two decay constants $T_f = 1.1$ ns and $T_s = 15.8$ ns gathered from a biexponential fit. The second-order correlation measurement under pulsed excitation is shown for $P/P_0 = 1$ and $P/P_0 = 0.02$ in Figs. 6(b) and (c), respectively. The solid red line represents the respective fit function.

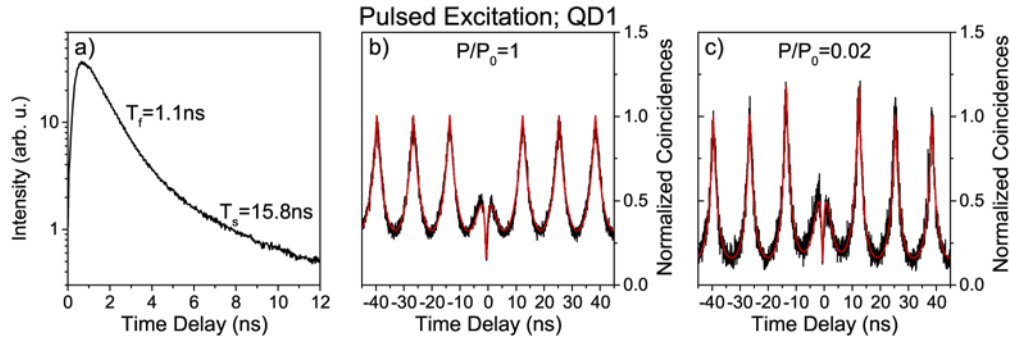


Fig. 6. Correlation measurements of the quantum dot labeled QD1 in the main text: (a) Time-resolved photoluminescence measurement in a semi-logarithmic plot. (b) and (c) Second-order correlation measurement under pulsed excitation for $P/P_0 = 1$ and $P/P_0 = 0.02$, respectively.

A.3. Experimental evaluation of the brightness

We define the brightness B as the ratio of the photons per time emitted by the sample and the number of excitation pulses per time. The charge carriers are excited optically in pulsed mode with a repetition rate of $r_{\text{laser}} = 76.9$ MHz and a central wavelength of 670 nm above the band gap of the barrier material (above-band). The brightness for a given NA is calculated by comparing the measured count rate at the detector with the repetition rate of the laser accounting for a non-ideal setup efficiency. The NA of the objective lens employed for this evaluation is 0.6. Assuming each excitation laser pulse triggers the emission of one photon the brightness is equal to the extraction efficiency. If the state preparation fidelity is unequal to unity or non-radiative decay channels are present, the above-mentioned assumption does not hold and the determined brightness will differ from the extraction efficiency [21].

Since under above-band excitation different excitonic states can form constituting corresponding decay channels for the charge carriers, the photons arising from parallel, i.e. non-consecutive channels, need to be added up [53]. In the present case, these are the photons arising from the recombination of the exciton (X), the trion (X^-) and the double negatively charged exciton (X^{2-}). To exclude any background contributions, the spectrum at saturation is fitted with Gaussian functions for the transitions and a constant offset for the background emission. To correct the measured counts for background contributions, a factor f_{bgc} is calculated from the area of the respective Gaussian function A_G and the constant offset A_{bg} within the spectral transmission window of the setup via

$$f_{\text{bgc}} = \frac{A_G}{A_G + A_{\text{bg}}}. \quad (1)$$

As discussed in the main text, a single excitation pulse can trigger more than one single-photon emission event due to refilling of the QD. To quantify this effect on the brightness [58], the pulsed second-order correlation measurement is fitted to extract the area of the central peak and the mean area of the outer peaks accounting for the temporal overlap and background contribution. The ratio of these areas $\tilde{g}_{\text{pulsed}}^{(2)}(0)$ (excluding overlapping pulses and background contributions) represents the probability for a secondary emission event in response to a single excitation pulse. This evaluation is performed for the X^{2-} and X^- transitions and yields $\tilde{g}_{\text{pulsed}}^{(2)}(0) = 0.69$ and $\tilde{g}_{\text{pulsed}}^{(2)}(0) = 0.73$ in saturation, respectively. Since due to a lower count rate this evaluation was not feasible for the X transition, the larger of the two previous values is assumed as a conservative estimate.

The setup efficiency η_{setup} is calculated from the individually measured transmission or reflection coefficients of the optical elements using a laser at the wavelength of the QD transition. The detector efficiency is measured by the manufacturer Scontel Superconducting Nanotechnology. The overall extraction efficiency is then calculated via

$$B = \frac{1}{r_{\text{laser}}\eta_{\text{setup}}} \cdot \sum_i r_{\text{raw},i} \cdot f_{\text{bgc},i} \cdot \sqrt{1 - \tilde{g}_{\text{pulsed},i}^{(2)}(0)}, \quad (2)$$

where the index i sums over all parallel decay channels and r_{raw} refers to the measured count rate at the detector.

Funding

Bundesministerium für Bildung und Forschung (16KIS0862, 16KIS0869); European Research Council (QD-NOMS GA715770); Deutsche Forschungsgemeinschaft (EXC-2123 390837967); Horizon 2020 Framework Programme (EMPIR 17FUN06 SIQUST).

Acknowledgments

The authors thank B. Eichler, R. Engelhard, and S. Baunack for their technical support. This work was funded by the Deutsche Forschungsgemeinschaft (DFG, German Research Foundation) under Germany's Excellence Strategy – EXC-2123 QuantumFrontiers – 390837967. This project received funding from the EMPIR programme cofinanced by the Participating States and from the European Union's Horizon 2020 research and innovation program.

Disclosures

The authors declare no conflicts of interest.

References

1. H. J. Kimble, "The quantum internet," *Nature* **453**(7198), 1023–1030 (2008).
2. A. K. Ekert, "Quantum cryptography based on bell's theorem," *Phys. Rev. Lett.* **67**(6), 661–663 (1991).
3. J.-W. Pan, Z.-B. Chen, C.-Y. Lu, H. Weinfurter, A. Zeilinger, and M. Żukowski, "Multiphoton entanglement and interferometry," *Rev. Mod. Phys.* **84**(2), 777–838 (2012).
4. M. Zopf, R. Keil, Y. Chen, J. Yang, D. Chen, F. Ding, and O. G. Schmidt, "Entanglement swapping with semiconductor-generated photons violates bell's inequality," *Phys. Rev. Lett.* **123**(16), 160502 (2019).
5. J.-H. Kim, T. Cai, C. J. Richardson, R. P. Leavitt, and E. Waks, "Two-photon interference from a bright single-photon source at telecom wavelengths," *Optica* **3**(6), 577–584 (2016).
6. J. Huwer, R. Stevenson, J. Skiba-Szymanska, M. Ward, A. Shields, M. Felle, I. Farrer, D. A. Ritchie, and R. V. Pentz, "Quantum-dot-based telecommunication-wavelength quantum relay," *Phys. Rev. Appl.* **8**(2), 024007 (2017).
7. M. Sartison, L. Engel, S. Kolatschek, F. Olbrich, C. Nawrath, S. Hepp, M. Jetter, P. Michler, and S. L. Portalupi, "Deterministic integration and optical characterization of telecom O-band quantum dots embedded into wet-chemically etched gaussian-shaped microlenses," *Appl. Phys. Lett.* **113**(3), 032103 (2018).
8. Ł. Dusanowski, P. Holewa, A. Maryński, A. Musiał, T. Heuser, N. Srocka, D. Quandt, A. Strittmatter, S. Rodt, J. Misiewicz, S. Reitzenstein, and G. Şek, "Triggered high-purity telecom-wavelength single-photon generation from p-shell-driven InGaAs/GaAs quantum dot," *Opt. Express* **25**(25), 31122–31129 (2017).
9. Z.-S. Chen, B. Ma, X.-J. Shang, H.-Q. Ni, J.-L. Wang, and Z.-C. Niu, "Bright single-photon source at 1.3 μm based on InAs bilayer quantum dot in micropillar," *Nanoscale Res. Lett.* **12**(1), 378 (2017).
10. M. Ward, O. Karimov, D. Unitt, Z. Yuan, P. See, D. Gevaux, A. Shields, P. Atkinson, and D. Ritchie, "On-demand single-photon source for 1.3 μm telecom fiber," *Appl. Phys. Lett.* **86**(20), 201111 (2005).
11. T. Miyazawa, K. Takemoto, Y. Nambu, S. Miki, T. Yamashita, H. Terai, M. Fujiwara, M. Sasaki, Y. Sakuma, M. Takatsu, T. Yamamoto, and Y. Arakawa, "Single-photon emission at 1.5 μm from an InAs/InP quantum dot with highly suppressed multi-photon emission probabilities," *Appl. Phys. Lett.* **109**(13), 132106 (2016).
12. M. Paul, F. Olbrich, J. Höschle, S. Schreier, J. Kettler, S. L. Portalupi, M. Jetter, and P. Michler, "Single-photon emission at 1.55 μm from MOVPE-grown InAs quantum dots on InGaAs/GaAs metamorphic buffers," *Appl. Phys. Lett.* **111**(3), 033102 (2017).
13. F. Olbrich, J. Höschle, M. Müller, J. Kettler, S. Luca Portalupi, M. Paul, M. Jetter, and P. Michler, "Polarization-entangled photons from an InGaAs-based quantum dot emitting in the telecom C-band," *Appl. Phys. Lett.* **111**(13), 133106 (2017).

14. T. Müller, J. Skiba-Szymanska, A. Krysa, J. Huwer, M. Felle, M. Anderson, R. Stevenson, J. Heffernan, D. A. Ritchie, and A. Shields, "A quantum light-emitting diode for the standard telecom window around 1,550 nm," *Nat. Commun.* **9**(1), 862 (2018).
15. M. Benyoucef, M. Yacob, J. Reithmaier, J. Kettler, and P. Michler, "Telecom-wavelength (1.5 μm) single-photon emission from InP-based quantum dots," *Appl. Phys. Lett.* **103**(16), 162101 (2013).
16. K. D. Zeuner, K. D. Jöns, L. Schweickert, C. R. Hedlund, C. N. Lobato, T. Lettner, K. Wang, S. Gyger, E. Schöll, S. Steinhauer, M. Hammar, and V. Zwiller, "On-demand generation of entangled photon pairs in the telecom C-band for fiber-based quantum networks," arXiv preprint arXiv:1912.04782 (2019).
17. M. Anderson, T. Müller, J. Huwer, J. Skiba-Szymanska, A. B. Krysa, R. M. Stevenson, J. Heffernan, D. A. Ritchie, and A. J. Shields, "Quantum teleportation using highly coherent emission from telecom C-band quantum dots," *npj Quantum Inf.* **6**(1), 14 (2020).
18. G. P. Agrawal, *Fiber-optic communication systems* (John Wiley & Sons, 2012).
19. A. Beveratos, S. Kühn, R. Brouri, T. Gacoin, J.-P. Poizat, and P. Grangier, "Room temperature stable single-photon source," *Eur. Phys. J. D* **18**(2), 191–196 (2002).
20. J. Hadden, J. Harrison, A. Stanley-Clarke, L. Marseglia, Y.-L. Ho, B. Patton, J. O'Brien, and J. Rarity, "Strongly enhanced photon collection from diamond defect centers under microfabricated integrated solid immersion lenses," *Appl. Phys. Lett.* **97**(24), 241901 (2010).
21. P. Michler, *Quantum dots for quantum information technologies* (Springer, 2017).
22. O. Gazzano, S. M. De Vasconcellos, C. Arnold, A. Nowak, E. Galopin, I. Sagnes, L. Lanco, A. Lemaître, and P. Senellart, "Bright solid-state sources of indistinguishable single photons," *Nat. Commun.* **4**(1), 1425 (2013).
23. S. Unsleber, Y.-M. He, S. Gerhardt, S. Maier, C.-Y. Lu, J.-W. Pan, N. Gregersen, M. Kamp, C. Schneider, and S. Höfling, "Highly indistinguishable on-demand resonance fluorescence photons from a deterministic quantum dot micropillar device with 74% extraction efficiency," *Opt. Express* **24**(8), 8539–8546 (2016).
24. X. Ding, Y. He, Z.-C. Duan, N. Gregersen, M.-C. Chen, S. Unsleber, S. Maier, C. Schneider, M. Kamp, S. Höfling, C.-Y. Lu, and J.-W. Pan, "On-demand single photons with high extraction efficiency and near-unity indistinguishability from a resonantly driven quantum dot in a micropillar," *Phys. Rev. Lett.* **116**(2), 020401 (2016).
25. N. Somaschi, V. Giesz, L. De Santis, J. C. Loredó, M. P. Almeida, G. Hornecker, S. L. Portalupi, T. Grange, C. Antón, J. Demory, C. Gómez, I. Sagnes, N. D. Lanzillotti-Kimura, A. Lemaître, A. Auffèves, A. G. White, L. Lanco, and P. Senellart, "Near-optimal single-photon sources in the solid state," *Nat. Photonics* **10**(5), 340–345 (2016).
26. M. Davanço, M. T. Rakher, D. Schuh, A. Badolato, and K. Srinivasan, "A circular dielectric grating for vertical extraction of single quantum dot emission," *Appl. Phys. Lett.* **99**(4), 041102 (2011).
27. L. Sapienza, M. Davanço, A. Badolato, and K. Srinivasan, "Nanoscale optical positioning of single quantum dots for bright and pure single-photon emission," *Nat. Commun.* **6**(1), 7833 (2015).
28. J. Liu, R. Su, Y. Wei, B. Yao, S. F. C. d. Silva, Y. Yu, J. Iles-Smith, K. Srinivasan, A. Rastelli, J. Li, and X. Wang, "A solid-state source of strongly entangled photon pairs with high brightness and indistinguishability," *Nat. Nanotechnol.* **14**(6), 586–593 (2019).
29. H. Wang, H. Hu, T.-H. Chung, J. Qin, X. Yang, J.-P. Li, R.-Z. Liu, H.-S. Zhong, Y.-M. He, X. Ding, Y.-H. Deng, Q. Dai, Y.-H. Huo, S. Höfling, C.-Y. Lu, and J.-W. Pan, "On-demand semiconductor source of entangled photons which simultaneously has high fidelity, efficiency, and indistinguishability," *Phys. Rev. Lett.* **122**(11), 113602 (2019).
30. J. Bleuse, J. Claudon, M. Creasey, N. S. Malik, J.-M. Gérard, I. Maksymov, J.-P. Hugonin, and P. Lalanne, "Inhibition, enhancement, and control of spontaneous emission in photonic nanowires," *Phys. Rev. Lett.* **106**(10), 103601 (2011).
31. M. E. Reimer, G. Bulgarini, N. Akopian, M. Hocevar, M. B. Bavinck, M. A. Verheijen, E. P. Bakkers, L. P. Kouwenhoven, and V. Zwiller, "Bright single-photon sources in bottom-up tailored nanowires," *Nat. Commun.* **3**(1), 737 (2012).
32. X.-W. Chen, S. Götzinger, and V. Sandoghdar, "99% efficiency in collecting photons from a single emitter," *Opt. Lett.* **36**(18), 3545–3547 (2011).
33. A. Schlehahn, M. Gaafar, M. Vaupel, M. Gschrey, P. Schnauber, J.-H. Schulze, S. Rodt, A. Strittmatter, W. Stolz, A. Rahimi-Iman, T. Heindel, M. Koch, and S. Reitzenstein, "Single-photon emission at a rate of 143 MHz from a deterministic quantum-dot microlens triggered by a mode-locked vertical-external-cavity surface-emitting laser," *Appl. Phys. Lett.* **107**(4), 041105 (2015).
34. M. Gschrey, A. Thoma, P. Schnauber, M. Seifried, R. Schmidt, B. Wohlfeil, L. Krüger, J. H. Schulze, T. Heindel, S. Burger, F. Schmidt, A. Strittmatter, S. Rodt, and S. Reitzenstein, "Highly indistinguishable photons from deterministic quantum-dot microlenses utilizing three-dimensional in situ electron-beam lithography," *Nat. Commun.* **6**(1), 7662 (2015).
35. S. Morozov, M. Gaio, S. A. Maier, and R. Sapienza, "Metal–dielectric parabolic antenna for directing single photons," *Nano Lett.* **18**(5), 3060–3065 (2018).
36. H. Galal and M. Agio, "Highly efficient light extraction and directional emission from large refractive-index materials with a planar yagi-uda antenna," *Opt. Mater. Express* **7**(5), 1634–1646 (2017).
37. F. Bigourdan, F. Marquier, J.-P. Hugonin, and J.-J. Greffet, "Design of highly efficient metallo-dielectric patch antennas for single-photon emission," *Opt. Express* **22**(3), 2337–2347 (2014).
38. A. Dousse, L. Lanco, J. Suffczynski, E. Semenova, A. Miard, A. Lemaître, I. Sagnes, C. Roblin, J. Bloch, and P. Senellart, "Controlled light-matter coupling for a single quantum dot embedded in a pillar microcavity using far-field optical lithography," *Phys. Rev. Lett.* **101**(26), 267404 (2008).

39. S. Ates, L. Sapienza, M. Davanco, A. Badolato, and K. Srinivasan, "Bright single-photon emission from a quantum dot in a circular Bragg grating microcavity," *IEEE J. Sel. Top. Quantum Electron.* **18**(6), 1711–1721 (2012).
40. Y. Chen, M. Zopf, R. Keil, F. Ding, and O. G. Schmidt, "Highly-efficient extraction of entangled photons from quantum dots using a broadband optical antenna," *Nat. Commun.* **9**(1), 2994 (2018).
41. S. Haffouz, K. D. Zeuner, D. Dalacu, P. J. Poole, J. Lapointe, D. Poitras, K. Mnaymneh, X. Wu, M. Couillard, M. Korkusinski, E. Schöll, K. D. Jöns, V. Zwiller, and R. L. Williams, "Bright single InAsP quantum dots at telecom wavelengths in position-controlled InP nanowires: the role of the photonic waveguide," *Nano Lett.* **18**(5), 3047–3052 (2018).
42. J. H. Weber, B. Kambs, J. Kettler, S. Kern, J. Maisch, H. Vural, M. Jetter, S. L. Portalupi, C. Becher, and P. Michler, "Two-photon interference in the telecom C-band after frequency conversion of photons from remote quantum emitters," *Nat. Nanotechnol.* **14**(1), 23–26 (2019).
43. H. Vural, S. L. Portalupi, J. Maisch, S. Kern, J. H. Weber, M. Jetter, J. Wrachtrup, R. Löw, I. Gerhardt, and P. Michler, "Two-photon interference in an atom–quantum dot hybrid system," *Optica* **5**(4), 367–373 (2018).
44. N. Srocka, A. Musiał, P.-I. Schneider, P. Mrowiński, P. Holewa, S. Burger, D. Quandt, A. Strittmatter, S. Rodt, S. Reitzenstein, and G. Şek, "Enhanced photon-extraction efficiency from InGaAs/GaAs quantum dots in deterministic photonic structures at 1.3 μm fabricated by in-situ electron-beam lithography," *AIP Adv.* **8**(8), 085205 (2018).
45. M. Paul, J. Kettler, K. Zeuner, C. Clausen, M. Jetter, and P. Michler, "Metal-organic vapor-phase epitaxy-grown ultra-low density InGaAs/GaAs quantum dots exhibiting cascaded single-photon emission at 1.3 μm ," *Appl. Phys. Lett.* **106**(12), 122105 (2015).
46. B. Höfer, F. Olbrich, J. Kettler, M. Paul, J. Höschele, M. Jetter, S. L. Portalupi, F. Ding, P. Michler, and O. G. Schmidt, "Tuning emission energy and fine structure splitting in quantum dots emitting in the telecom O-band," *AIP Adv.* **9**(8), 085112 (2019).
47. J. Zhang, F. Ding, E. Zallo, R. Trotta, B. Höfer, L. Han, S. Kumar, Y. Huo, A. Rastelli, and O. G. Schmidt, "A nanomembrane-based wavelength-tunable high-speed single-photon-emitting diode," *Nano Lett.* **13**(12), 5808–5813 (2013).
48. J. Kettler, M. Paul, F. Olbrich, K. Zeuner, M. Jetter, and P. Michler, "Single-photon and photon pair emission from MOVPE-grown In(Ga)As quantum dots: shifting the emission wavelength from 1.0 to 1.3 μm ," *Appl. Phys. B* **122**(3), 48 (2016).
49. J. Kettler, M. Paul, F. Olbrich, K. Zeuner, M. Jetter, P. Michler, M. Florian, C. Carmesin, and F. Jahnke, "Neutral and charged biexciton-exciton cascade in near-telecom-wavelength quantum dots," *Phys. Rev. B* **94**(4), 045303 (2016).
50. T. Aichele, V. Zwiller, and O. Benson, "Visible single-photon generation from semiconductor quantum dots," *New J. Phys.* **6**, 90 (2004).
51. P. A. Dalgarno, J. McFarlane, D. Brunner, R. W. Lambert, B. D. Gerardot, R. J. Warburton, K. Karrai, A. Badolato, and P. M. Petroff, "Hole recapture limited single photon generation from a single n-type charge-tunable quantum dot," *Appl. Phys. Lett.* **92**(19), 193103 (2008).
52. H. Kumano, T. Harada, I. Suemune, H. Nakajima, T. Kuroda, T. Mano, K. Sakoda, S. Odashima, and H. Sasakura, "Stable and efficient collection of single photons emitted from a semiconductor quantum dot into a single-mode optical fiber," *Appl. Phys. Express* **9**(3), 032801 (2016).
53. S. Fischbach, A. Schlehahn, A. Thoma, N. Srocka, T. Gissibl, S. Ristok, S. Thiele, A. Kaganskiy, A. Strittmatter, T. Heindel, S. Rodt, A. Herkommer, H. Giessen, and S. Reitzenstein, "Single quantum dot with microlens and 3D-printed micro-objective as integrated bright single-photon source," *ACS Photonics* **4**(6), 1327–1332 (2017).
54. G. Sallen, A. Tribu, T. Aichele, R. André, L. Besombes, C. Bougerol, M. Richard, S. Tatarenko, K. Kheng, and J.-P. Poizat, "Subnanosecond spectral diffusion measurement using photon correlation," *Nat. Photonics* **4**(10), 696–699 (2010).
55. J. Kettler, "Telecom-wavelength nonclassical light from single In(Ga)As quantum dots," Ph.D. thesis, Universität Stuttgart (2016).
56. E. Peter, S. Laurent, J. Bloch, J. Hours, S. Varoutsis, I. Robert-Philip, A. Beveratos, A. Lemàtre, A. Cavanna, G. Patriarche, P. Senellart, and D. Martrou, "Fast radiative quantum dots: From single to multiple photon emission," *Appl. Phys. Lett.* **90**(22), 223118 (2007).
57. P. Michler, A. Imamoglu, M. D. Mason, P. J. Carson, G. F. Strouse, and S. K. Buratto, "Quantum correlation among photons from a single quantum dot at room temperature," *Nature* **406**(6799), 968–970 (2000).
58. M. Pelton, C. Santori, J. Vučković, B. Zhang, G. S. Solomon, J. Plant, and Y. Yamamoto, "Efficient source of single photons: a single quantum dot in a micropost microcavity," *Phys. Rev. Lett.* **89**(23), 233602 (2002).
59. S. Adachi, "Optical dispersion relations for GaP, GaAs, GaSb, InP, InAs, InSb, $\text{Al}_x\text{Ga}_{1-x}\text{As}$, and $\text{In}_{1-x}\text{Ga}_x\text{As}_y\text{P}_{1-y}$," *J. Appl. Phys.* **66**(12), 6030–6040 (1989).
60. J. Yang, T. Wang, Z. Chen, B. Hu, and W. Yu, "Super-resolution imaging at mid-infrared waveband in graphene-nanocavity formed on meta-surface," *Sci. Rep.* **6**(1), 37898 (2016).